System-size dependence of Λ and Ξ production in nucleus–nucleus collisions at 40A and 158A GeV measured at the CERN Super Proton Synchrotron

T. Anticic,[23] B. Baatar,[8] D. Barna,[4] J. Bartke,[6] H. Beck,[9] L. Betev,[10] H. Białkowska,[20] C. Blume,[9] B. Boimska,[20] J. Book,[9] M. Botje,[1] J. Bracinik,[3] P. Bunčić,[10] V. Cerny,[3] P. Christakoglou,[1] P. Chung,[19] O. Chvala,[14] J.G. Cramer,[16] P. Csató,[4] P. Dinkelaker,[9] V. Eckardt,[13] Z. Fodor,[4] P. Foka,[7] V. Friese,[7] J. Gál,[4] M. Gaździcki,[9,11] V. Genchev,[18] K. Grebieszkow,[22] S. Hegyi,[4] C. Höhne,[7] K. Kadija,[23] A. Karev,[13] D. Kresan,[7] V.I. Kolesnikov,[8] M. Kowalski,[6] I. Kraus,[7] M. Kreps,[3] A. Laszlo,[4] R. Lacey,[19] M. van Leeuwen,[1] P. Lévai,[4] L. Litov,[17] B. Lungwitz,[9] M. Makariev,[18] A.I. Malakhov,[8] M. Mateev,[17] G.L. Melkumov,[8] C. Meurer,[9] A. Mischke,[1] M. Mitrovski,[9] J. Molnár,[4] St. Mrówczyński,[11] V. Nicolic,[23] G. Pálla,[4] A.D. Panagiotou,[2] D. Panayotov,[17] A. Petridis,[2,*] W. Peryt,[22] M. Pikna,[3] J. Pluta,[22] D. Prindle,[16] F. Pühlhofer,[12] R. Renfordt,[9] C. Roland,[5] G. Roland,[5] M. Rybczyński,[11] A. Rybicki,[6] A. Sandoval,[7] N. Schmitz,[13] T. Schuster,[9] P. Seyboth,[13] F. Siklér,[4] B. Sitar,[3] E. Skrzypczak,[21] M. Slodkowski,[22] G. Stefanek,[11] R. Stock,[9] C. Strabel,[9] H. Ströbele,[9] T. Susa,[23] I. Szentpétery,[4] J. Sziklai,[4] M. Szuba,[22] P. Szymanski,[20] M. Utvić,[9] D. Varga,[4,10] M. Vassiliou,[2] G.I. Veres,[4,5] G. Vesztergombi,[4] D. Vranić,[7] Z. Włodarczyk,[11] A. Wojtaszek,[11] and I.K. Yoo[15]

(The NA49 Collaboration)

[1] *NIKHEF, Amsterdam, Netherlands.*
[2] *Department of Physics, University of Athens, Athens, Greece.*
[3] *Comenius University, Bratislava, Slovakia.*
[4] *KFKI Research Institute for Particle and Nuclear Physics, Budapest, Hungary.*
[5] *MIT, Cambridge, USA.*
[6] *Henryk Niewodniczanski Institute of Nuclear Physics, Polish Academy of Sciences, Cracow, Poland.*
[7] *Gesellschaft für Schwerionenforschung (GSI), Darmstadt, Germany.*
[8] *Joint Institute for Nuclear Research, Dubna, Russia.*
[9] *Fachbereich Physik der Universität, Frankfurt, Germany.*
[10] *CERN, Geneva, Switzerland.*
[11] *Institute of Physics Świętokrzyska Academy, Kielce, Poland.*
[12] *Fachbereich Physik der Universität, Marburg, Germany.*
[13] *Max-Planck-Institut für Physik, Munich, Germany.*
[14] *Charles University, Faculty of Mathematics and Physics, Institute of Particle and Nuclear Physics, Prague, Czech Republic.*
[15] *Department of Physics, Pusan National University, Pusan, Republic of Korea.*
[16] *Nuclear Physics Laboratory, University of Washington, Seattle, WA, USA.*
[17] *Atomic Physics Department, Sofia University St. Kliment Ohridski, Sofia, Bulgaria.*
[18] *Institute for Nuclear Research and Nuclear Energy, Sofia, Bulgaria.*
[19] *Department of Chemistry, Stony Brook Univ. (SUNYSB), Stony Brook, USA.*
[20] *Institute for Nuclear Studies, Warsaw, Poland.*
[21] *Institute for Experimental Physics, University of Warsaw, Warsaw, Poland.*
[22] *Faculty of Physics, Warsaw University of Technology, Warsaw, Poland.*
[23] *Rudjer Boskovic Institute, Zagreb, Croatia.*

Results on Λ, $\bar{\Lambda}$, and Ξ^- production in centrality selected Pb+Pb reactions at 40A and 158A GeV and in near-central C+C and Si+Si reactions at 158A GeV are presented. Transverse mass spectra, rapidity spectra, and multiplicities in dependence of the system size are discussed. Comparisons to transport models (UrQMD2.3 and HSD) and to the core-corona approach are performed. While Λ and $\bar{\Lambda}$ production can be described by transport models reasonably well, these models do not agree with the Ξ^- measurements. On the other hand, the core-corona picture fits very well the system-size dependence of Λ and Ξ^-, while it agrees less well with the $\bar{\Lambda}$ data.

I. INTRODUCTION

The production of strange particles has always been a key observable in heavy-ion reactions and its enhancement was one of the first suggested signatures for quark-gluon plasma (QGP) formation [1]. The predicted enhancement of strangeness production in nucleus–nucleus collisions relative to proton–proton reactions was established experimentally some time ago [2, 3]. It was also found that this enhancement is increasing with the strangeness content of the particle type [4, 5].

However, there are several aspects that make a straightforward interpretation of the experimental results difficult. One of them is the fact, that the strangeness enhancement seems to increase towards lower energies [6, 7, 8]. Another open issue and the topic of this pub-

*deceased

lication is the dependence of the enhancement on the system size. The latter is quantified by the number of "wounded" nucleons from the colliding nuclei that participate in the reaction. A previous analysis investigated the pion, kaon, ϕ, and Λ production in (near-)central nucleus–nucleus collisions of nuclei with different mass numbers [9]. It turned out that the enhancement sets in already for very small systems and seems to saturate for nuclei with mass number above 30, i. e. number of participants above 60. The present study extends the investigation of the enhancement to non-central Pb+Pb collisions and to the production of $\bar{\Lambda}$ and Ξ^- hyperons.

In the context of statistical models, which generally have been quite successful in describing particles yields, the experimentally observed strangeness enhancement for large systems is due to the increase of the reaction volume, which weakens the influence of strangeness conservation on the production rate [10]. In [11] this has been modeled by the transition from a canonical ensemble to a grand-canonical one. For comparison of the corresponding statistical model results to experimental data, the relation between the size of the ensemble volume V and the experimentally accessible number of wounded nucleons $\langle N_{\rm w}\rangle$ has been assumed to be $V = (V_0/2)\,\langle N_{\rm w}\rangle$. The parameter V_0, which accounts for the locality of the strangeness conservation, is usually fixed to ≈ 7 fm^3 [11]. However, this approach does not provide a satisfactory description of the data [9]. A better agreement with global strangeness production at the SPS can be achieved by deriving the ensemble volume from a percolation of elementary clusters [12]. A similar, although simplified, line of argument is put forward in the so-called core-corona picture [13]. Here a heavy-ion collision is considered a superposition of a hot and dense core and a low density peripheral corona region. While the core region corresponds to a large fireball, which experiences collective expansion and for which particle production should be describable via a large volume canonical ensemble, or equivalently by a grand-canonical statistical ensemble, the corona is supposed to exhibit the features of simple nucleon-nucleon collisions. The contributions of the core and the corona depend on both the size of the colliding nuclei and the centrality of the collision and can be determined via Glauber model calculations [14]. This concept has recently been applied quite successfully to the system-size dependence of strangeness production at RHIC energies [15, 16, 17, 18].

The comparison of measurements with hadron–string transport models, such as UrQMD or HSD, provides insight into the question whether nucleus–nucleus collisions can be described in a hadronic scenario or whether a contribution from an additional partonic phase is needed. Even though these models are not able to describe the enhancement of multi-strange particle yields in central nucleus–nucleus collisions [8], their predictions are generally close to the measured values for particles containing a single strange quark. Their comparison to the measured system-size dependence might therefore reveal effects that go beyond the dominating influence of the reaction geometry, such as multi-pion fusion processes and, in the case of anti-baryons, absorption in dense nuclear matter.

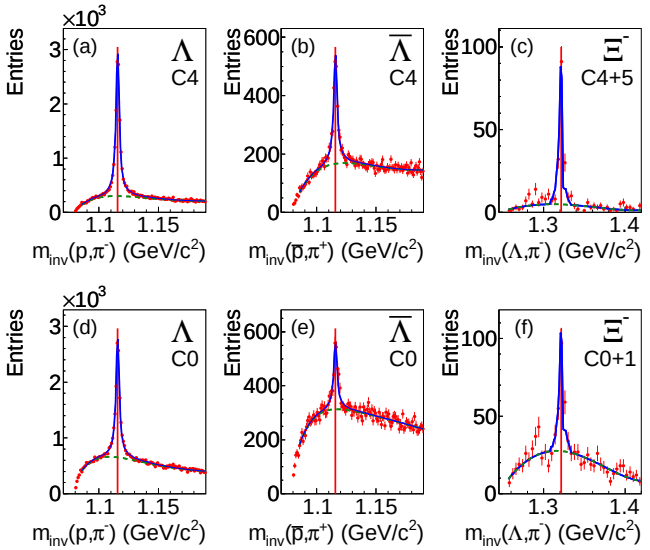

FIG. 1: (color online) The invariant mass distributions of all measured Λ, $\bar{\Lambda}$, and Ξ^- candidates in two centrality classes of Pb+Pb collisions at 158A GeV. The upper row (a – c) shows the most peripheral centrality class, the lower row (d – f) the most central one. The full curves represent a fit to signal and background as described in the text, while the dashed curves show the background only. The vertical lines denote the literature values of the masses [20].

II. DATA ANALYSIS

A. Experimental setup and data sets

The data were taken with the NA49 large acceptance hadron spectrometer at the CERN SPS. A detailed description of the apparatus can be found in [19]. With this detector tracking is performed by four large-volume Time Projection Chambers (TPCs) in a wide range of phase space. Two of these are positioned inside two superconducting dipole magnets. In order to ensure a similar detector acceptance in the center-of-mass system for all datasets, the magnetic field was reduced for the 40A GeV Pb beam by a factor of 4. A measurement of the specific energy loss dE/dx in the TPC gas with a typical resolution of 4 % provides particle identification at forward rapidities. Time-of-flight detectors improve the particle identification at mid-rapidity. The centrality of a given reaction is determined via the energy measured in the projectile fragmentation region by the Zero Degree Calorimeter (ZDC) positioned downstream of the TPCs. A collimator in front of the ZDC reduces the acceptance

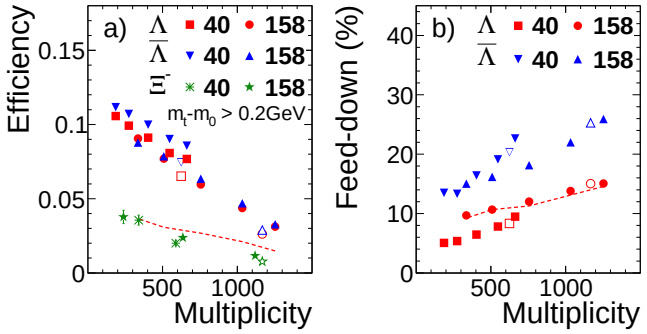

FIG. 2: (color online) The p_t-integrated reconstruction efficiency (a) and feed-down contribution (b) at mid-rapidity (Λ, $\bar{\Lambda}$: $|y| < 0.4$, Ξ^-: $|y| < 0.5$) as a function of centrality as characterized by the measured charged track multiplicity for minimum bias Pb+Pb reactions at 40A and 158A GeV. Open symbols correspond to the values for central Pb+Pb collisions [8]. The dashed lines represent the Λ efficiency or feed-down contribution respectively, at 158A GeV, resulting from a different analysis strategy (see text).

of the calorimeter to the phase space of the projectile fragments and spectator nucleons.

We present in this paper an analysis of centrality selected Pb+Pb events taken with a minimum bias trigger at beam energies of 40A and 158A GeV in the years 1999 and 2000, and of near-central C+C and Si+Si events measured at 158A GeV in the year 1998. The properties of the different datasets are summarized in Tables I and II. While for the Pb+Pb collisions the primary SPS beam was used, the C and Si ions were created by fragmenting the original Pb beam. By tuning the magnetic rigidity in the beam line ($Z/A = 0.5$) and analyzing the specific energy loss in scintillation detectors, the corresponding ion species could be selected. In the following, the carbon beam is defined as $Z = 6$ ions and the silicon beam as a mixture of $Z = 13 - 15$. Two carbon targets with thicknesses of 3 mm and 10 mm (561 mg/cm^2 and 1840 mg/cm^2, respectively) and a silicon target with a thickness of 5 mm (1170 mg/cm^2) were used. Further details on the analysis of the C+C and Si+Si datasets can be found in [9]. For the study of the minimum bias Pb+Pb interactions targets with a thickness of 200 μm (224 mg/cm^2) were installed. The minimum bias trigger is defined by a gas Cherenkov counter that vetoes non-interacting projectiles. Centrality classes C0 – C4 are defined by consecutive intervals of spectator energy as measured in the ZDC calorimeter. Simulated events from the VENUS 4.12 event generator [21] were used to relate this energy to the number of wounded nucleons $\langle N_w \rangle$ as given by the implemented Glauber model calculation [14]. The background from non-target interactions is substantially reduced by applying cuts on the reconstructed position of the primary vertex. After these cuts the centrality classes C0 – C2 are free of background events, while the more peripheral classes C3 and C4 have a contamination of less than 2 % and 5 %, respectively.

TABLE I: Summary of the analyzed Pb+Pb datasets. The centrality is quantified by the fraction of the total inelastic cross section. $\langle N_w \rangle$ is the average number of wounded nucleons per event and $\sigma(\langle N_w \rangle)$ the widths of the corresponding distributions. For the 158A GeV dataset also the fraction $f(\langle N_w \rangle)$ of nucleons that scatter more than once is given [18]. N_{Event} is the number of accepted events.

E_{beam} (A GeV)	Class	Centrality (%)	$\langle N_w \rangle$	$\sigma(\langle N_w \rangle)$	$f(\langle N_w \rangle)$	N_{Event}
40	C0	0.0 – 5.0	351±3	16±1	—	26k
	C1	5.0 – 12.5	290±4	21±2	—	45k
	C2	12.5 – 23.5	210±6	22±2	—	66k
	C3	23.5 – 33.5	142±8	22±3	—	62k
	C4	33.5 – 43.5	93±7	21±2	—	63k
158	C0	0.0 – 5.0	352±3	13±1	0.89	14k
	C1	5.0 – 12.5	281±4	18±2	0.85	23k
	C2	12.5 – 23.5	196±6	19±2	0.80	36k
	C3	23.5 – 33.5	128±8	19±3	0.74	33k
	C4	33.5 – 43.5	85±7	18±2	0.68	33k

TABLE II: Summary of the analyzed near-central C+C and Si+Si datasets. The centrality is quantified by the fraction of the total inelastic cross section. $\langle N_w \rangle$ is the average number of wounded nucleons per event and N_{Event} the number of accepted events.

E_{beam} (A GeV)	Reaction	Centrality (%)	$\langle N_w \rangle$	N_{Event}
158	C+C	0.0 – 15.3	14±2	250k
	Si+Si	0.0 – 12.2	37±3	200k

B. Λ, $\bar{\Lambda}$, and Ξ^- reconstruction

The reconstruction of Λ, $\bar{\Lambda}$, and Ξ^- follows the same procedures as employed in a previous analysis [8]. A detailed description of the methods, together with a list of all applied cuts, can thus be found there. Here we just summarize the basic principles.

Λ and $\bar{\Lambda}$ hyperons were reconstructed from their charged decays $\Lambda \rightarrow \pi^- + p$ and $\bar{\Lambda} \rightarrow \pi^+ + \bar{p}$ (branching ratio 63.9 % [20]). Candidate pairs were formed by combining all reconstructed tracks of positively with all tracks of negatively charged particles. Pairs with a distance of closest approach (DCA) of less than 0.5 cm anywhere between the position of the first measured points on the tracks and the target plane are treated as possible V^0 candidates. The (anti-)protons are identified via their specific energy loss (dE/dx) in the TPCs which removes the background resulting from a wrong mass assignment.

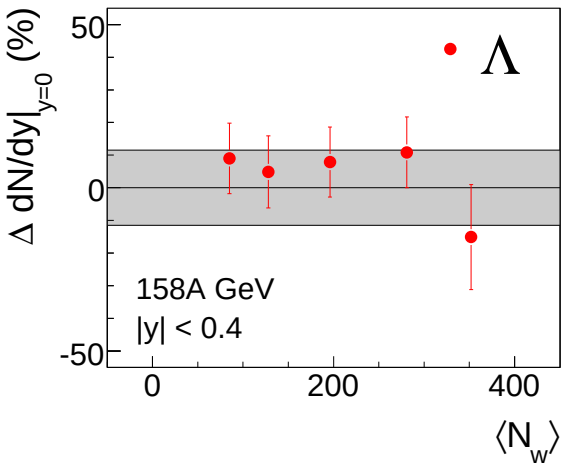

FIG. 3: (color online) The differences between the fully corrected dN/dy values at mid-rapidity for Λ at 158A GeV as extracted with the standard procedure and the alternative analysis strategy (see section II C) for the different centrality bins. The gray area illustrates the systematic error estimate.

The combinatorial background is further reduced by applying additional cuts to V^0 candidates. These include a minimal distance of the reconstructed decay vertex position to the main interaction vertex and the requirement that the reconstructed momentum vectors of the Λ ($\bar{\Lambda}$) candidates should point back to the interaction vertex. Due to the lower multiplicities in C+C and Si+Si reactions, the combinatorial background for Λ and $\bar{\Lambda}$ is much smaller. Therefore, the cuts have been relaxed compared to the ones in the analysis of the Pb+Pb data. Ξ^- candidates were identified via the decay channel $\Xi^- \rightarrow \Lambda + \pi^-$ which has a branching ratio of 99.9 % [20]. To reconstruct the Ξ^-, Λ candidates were selected in an invariant mass window of 1.101 – 1.131 GeV/c^2 and combined with all measured negatively charged particles in the event. The Λ candidates were subjected to the same selection criteria as used in the Λ analysis, except for the momentum pointing cut. The reconstructed Ξ^- candidates were required to point back to the interaction vertex. In order to further reduce the number of fake Ξ^-, the trajectories of the negatively charged pions from Λ and Ξ^- decays were intersected with the target plane and the distances of the resulting positions to the main interaction vertex were required to be larger than a minimum value.

The invariant mass spectra were measured in bins of p_t, $(m_t - m_0)$, y, as well as centrality, and fitted to the sum of a polynomial and a signal distribution, the latter determined from simulation. The raw yields of Λ, $\bar{\Lambda}$, and Ξ^- were obtained by subtracting the fitted background and integrating the remaining signal distributions in a mass window of ± 11 MeV/c^2 (± 10 MeV/c^2) around the nominal Λ (Ξ) mass. Typical mass resolutions for Λ (Ξ), as obtained from a fit with a Gaussian, are $\sigma_m \approx 2$ MeV/c^2 (4 MeV/c^2). Figure 1 shows examples of invariant mass distributions for two centrality classes of Pb+Pb collisions at 158A GeV together with the corresponding fitted curves.

C. Correction for acceptance, reconstruction inefficiency and feed-down

Detailed simulations were made to correct the yields for geometrical acceptance and inefficiencies of the reconstruction procedure. As input to these simulations samples of Λ, $\bar{\Lambda}$ and Ξ^- were generated with m_t distributions according to:

$$\frac{1}{m_t}\frac{dN}{dm_t} \propto \exp\left(-\frac{m_t}{T}\right). \quad (1)$$

Here p_t is the transverse momentum, $m_t = \sqrt{p_t^2 + m^2}$, and T the inverse slope parameter. In case of the Pb+Pb collisions the T parameter was determined by measurements for central Pb+Pb reactions [8], while for the C+C and Si+Si collisions T was set to 200 MeV. The rapidity spectra of $\bar{\Lambda}$ and Ξ^- for Pb+Pb reactions were modeled by single Gaussian distributions. The flatter Λ rapidity spectra were instead approximated by the sum of two (Pb+Pb at 40A GeV) or three (Pb+Pb at 158A GeV) Gaussians, respectively. For the C+C and Si+Si collisions the distributions for Λ and $\bar{\Lambda}$ were assumed to be constant as a function of rapidity. The Geant 3.21 package [22] was used to track the generated particles and their decay products through the NA49 detector. The TPC response, which takes into account all known detector effects, was simulated by software developed for the NA49 experiment. The simulated signals were added to those of real events on the raw data level and subjected to the same reconstruction procedure as the experimental data. By determining the fraction of the generated Λ, $\bar{\Lambda}$ and Ξ^- which traverse the detector, survive the reconstruction, and pass all analysis cuts, the combined acceptances and efficiencies were derived. The corresponding correction factors were calculated in bins of p_t, $(m_t - m_0)$, y, as well as centrality in the case of Pb+Pb collisions.

Figure 2a summarizes the centrality dependence of the efficiencies, including acceptance. While for Λ and $\bar{\Lambda}$ at 40A GeV only a 30 % variation can be observed, the difference between very peripheral and very central bins is a factor of 3 at 158A GeV. For the Λ also an alternative analysis strategy was employed: on top of the standard cuts, only those Λ were accepted whose daughter tracks lie entirely outside the high track density region (CUT-B in [8]). This reduces the overall efficiency, but has the benefit that the track multiplicity effects are slightly reduced compared to the standard analysis (see dashed line in Fig. 2a). The influence of the detector occupancy on the efficiency is much smaller for C+C and Si+Si reactions at 158A GeV. It was found that the reduction of the efficiency due to other tracks is ~ 5 % for Si+Si and negligible for C+C. Therefore, it was only corrected for

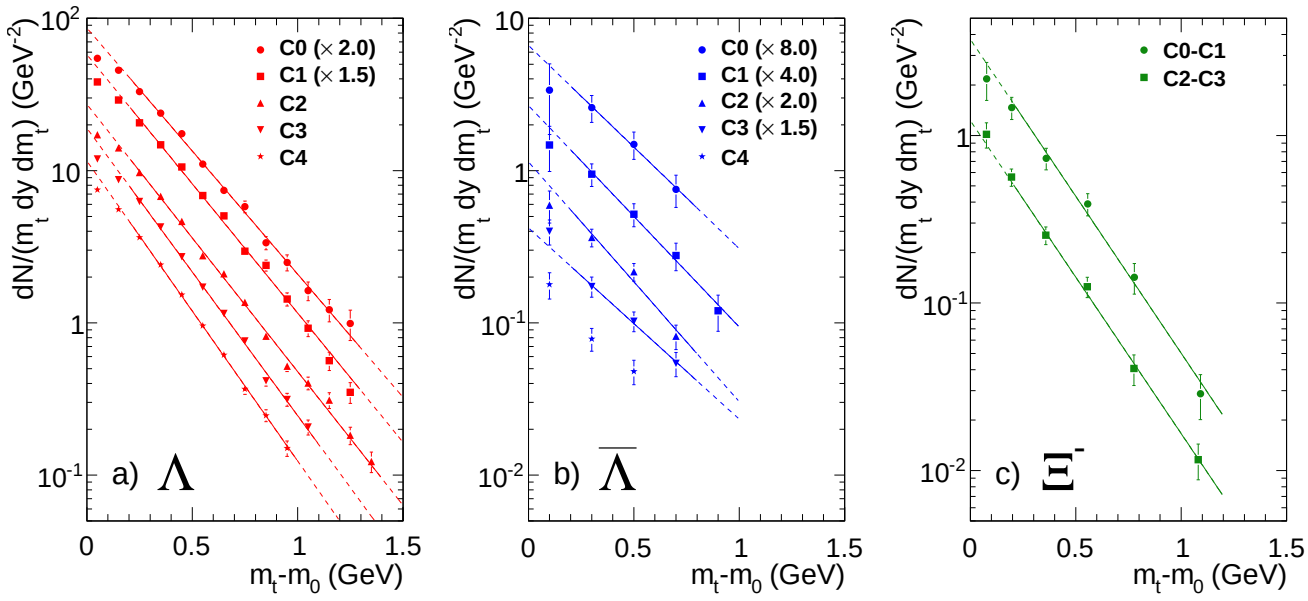

FIG. 4: (color online) The transverse mass spectra of Λ (a), $\bar{\Lambda}$ (b), and Ξ^- (c) at mid-rapidity ($\Lambda/\bar{\Lambda}$: $|y| < 0.4$, Ξ^-: $|y| < 0.5$) for Pb+Pb reactions at 40A GeV in different centrality bins. Some of the data points are scaled for clarity. Only statistical errors are shown. The solid/dashed lines represent fits with an exponential, where the solid parts denote the m_t ranges in which the fits were performed.

in the case of Si+Si reactions. Due to the relaxed analysis cuts, the efficiencies are generally higher for the small systems than for minimum bias Pb+Pb reactions ($\Lambda/\bar{\Lambda}$: $\sim$ 55 %, Ξ^-: $\sim$ 6 %, both mid-rapidity) [23, 24].

In addition to the directly produced particles, the measured yield of Λ and $\bar{\Lambda}$ contains also contributions from the decay of heavier hyperons. The Λ ($\bar{\Lambda}$) resulting from electromagnetic decays of Σ^0 ($\bar{\Sigma}^0$) cannot be separated from the directly produced ones via a secondary vertex measurement. Thus the presented yields always represent the sum $\Lambda+\Sigma^0$ ($\bar{\Lambda}+\bar{\Sigma}^0$). The contribution to Λ ($\bar{\Lambda}$) from weak decays, however, depends on the chosen analysis cuts, because these decay products originate from decay vertices with a sizable distance from the main interaction point. Since the NA49 acceptance for Λ ($\bar{\Lambda}$) favors those that decay at larger distances, the contribution of feed-down Λ ($\bar{\Lambda}$) can be quite substantial. Therefore, we calculated a correction for the feed-down from $\Xi^- + \Xi^0$ ($\bar{\Xi}^+ + \bar{\Xi}^0$) decays to the measured Λ ($\bar{\Lambda}$) sample using the same simulation procedure as described above for the efficiency correction. In this case a sample of Ξ^- and Ξ^0 ($\bar{\Xi}^+$ and $\bar{\Xi}^0$) was generated as input. The feed-down correction was then calculated in bins of p_t, $(m_t - m_0)$, y, as well as reaction centrality, as the fraction of reconstructed Λ ($\bar{\Lambda}$) which originate from $\Xi^- + \Xi^0$ ($\bar{\Xi}^+ + \bar{\Xi}^0$) decays and pass the same analysis cuts. The Ξ^- yields used as input to this procedure are based on the measurements presented in this publication, which were interpolated to all centrality bins. The extrapolation of the $\bar{\Xi}^+$ yields to the different centrality bins was based on the yield measured in central Pb+Pb reactions [8]. It was assumed that the centrality dependence of the $\bar{\Xi}^+$ yields is the same as measured for the Ξ^-. In both cases the shapes of the input rapidity and p_t distributions are a parametrization of the spectra measured for central collisions. For the Ξ^0 ($\bar{\Xi}^0$), which are not measured, the same shape of the phase space distributions as for the Ξ^- was assumed. Their yields are calculated by scaling those of Ξ^- ($\bar{\Xi}^+$) by the Ξ^0/Ξ^- ($\bar{\Xi}^0/\bar{\Xi}^+$) ratios taken from statistical model fits [25]. As an example, the p_t-integrated feed-down contribution around mid-rapidity is shown in Fig. 2b. Since the Ξ yields have a stronger centrality dependence than the Λ yields, the feed-down contribution changes with centrality. In the case of C+C and Si+Si reactions all yields entering the calculation of the feed-down are based on statistical model fits [25]. The parameters for their phase space distributions are adjusted such as to interpolate between p+p and Pb+Pb reactions. The corrections amount to 9 % (10 %) for Λ and 15 % (20 %) for $\bar{\Lambda}$ in C+C (Si+Si) [23].

D. Systematic errors

The contributions to the systematic error of the dN/dy values measured in centrality selected Pb+Pb reactions are listed in Table III. The first two, the uncertainty of the background subtraction and the efficiency correction, are identical to the ones determined for the analysis of the central Pb+Pb datasets [8]. However, there is a difference in the contribution from the feed-down correction to the systematic error in the central

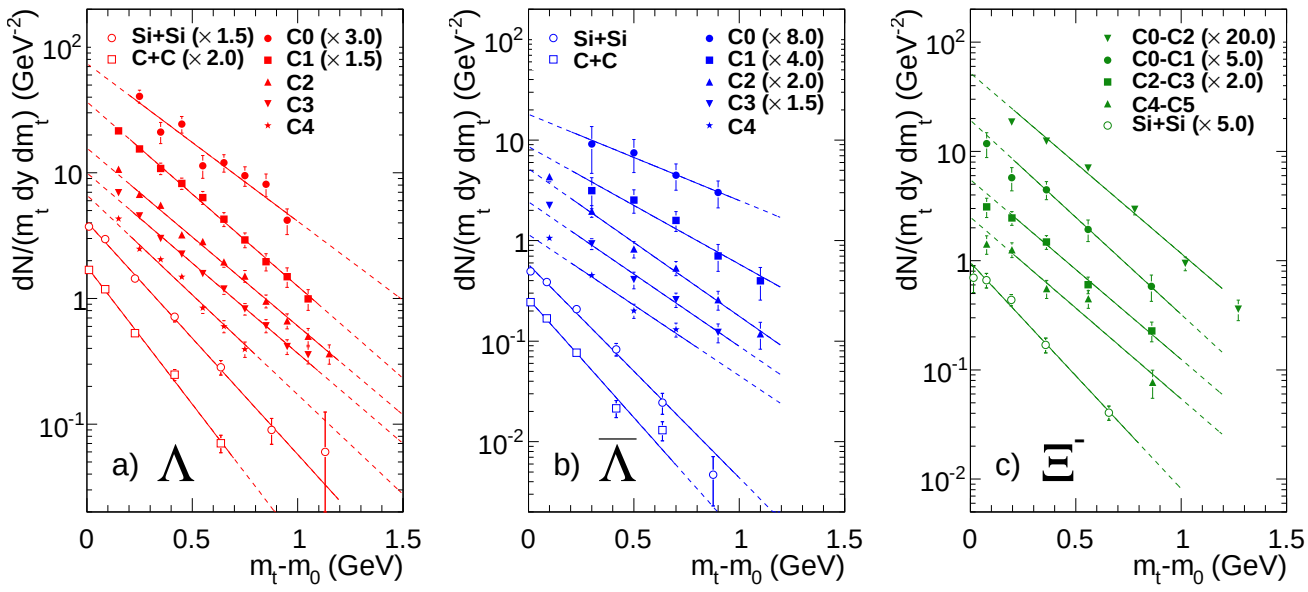

FIG. 5: (color online) The transverse mass spectra of Λ (a), $\bar{\Lambda}$ (b), and Ξ^- (c) at mid-rapidity ($\Lambda/\bar{\Lambda}$: $|y| < 0.4$, Ξ^-: $|y| < 0.5$) for Pb+Pb reactions at 158A GeV in different centrality bins, and in near-central C+C and Si+Si collisions at 158A GeV. Some of the data points are scaled for clarity. Only statistical errors are shown. The solid/dashed lines represent fits with an exponential, where the solid parts denote the m_t ranges in which the fits were performed. The Λ spectra for C+C and Si+Si are taken from [9].

TABLE III: Summary of the systematic errors on the dN/dy values for minimum bias Pb+Pb reactions.

	$E_{\rm beam}$ A GeV	Bgnd. subtr.	Eff. corr.	$p_{\rm t}$ Extrapolation	Feed. corr.	Quad. sum
Λ	40	3%	10%	—	3%	11%
	158			3%		11.5%
$\bar{\Lambda}$	40	3%	10%	—	8%	13%
	158			3%		13.5%
Ξ^-	40/158	3%	10%	3%	—	11%

Pb+Pb analysis. The yields of Ξ^- and particularly of $\bar{\Xi}^+$, are less precisely measured for non-central Pb+Pb reactions than for central ones. While the feed-down contribution from Ξ^- and Ξ^0 to Λ can still be constrained reasonably well with the measurement presented here, the feed-down estimate from $\bar{\Xi}^+$ and $\bar{\Xi}^0$ to $\bar{\Lambda}$ relies on an extrapolation of the measurement in central collisions assuming the same centrality dependence. By varying the Ξ input yields inside the errors obtained for the central data set and assuming different centrality dependences (e.g. scaling with $\langle N_{\rm w} \rangle$) the contribution to the systematic error was evaluated. As a result a systematic error of 3 % was assigned to the Λ, while for the $\bar{\Lambda}$ it is 8 %. Since the minimum bias data at 158A GeV, and for Ξ^- also at 40A GeV, do not allow to measure the $p_{\rm t}$-range down to $p_{\rm t} = 0$ GeV/c, an extrapolation has to be used. By comparing the result for the standard fit (exponential, as shown in Figs. 4 and 5) to an extrapolation using a fit with a hydrodynamically inspired blast-wave model [26], a systematic error of 3 % was determined for these cases. Figure 3 demonstrates the consistency of the systematic error estimated for the Λ yield with the spread of results obtained from the two analysis strategies discussed above.

The extrapolations in rapidity, which are needed to extract the total multiplicities, introduce additional systematic errors. The data allow to constrain the widths of the fits, as shown in Figs. 7 and 8, only to a certain extent which translates into an uncertainty of the extrapolation. In the case of Λ at 158A GeV, the shapes of the rapidity distributions are not measured. Therefore a set of assumptions based on other measurements as discussed in [8] was used. The shaded areas in Fig. 8 represent the uncertainty of the extrapolations that were included in the systematic error.

III. RESULTS

A. Transverse mass spectra

The transverse mass spectra of Λ, $\bar{\Lambda}$, and Ξ^-, measured around mid-rapidity ($\Lambda/\bar{\Lambda}$: $|y| < 0.4$, Ξ^-: $|y| < 0.5$), are shown for different centrality classes of minimum bias Pb+Pb collisions at 40A GeV in Fig. 4 and at 158A GeV in Fig. 5. Also included in Fig. 5 are the $m_{\rm t}$ spectra for near-central C+C and Si+Si reactions at 158A GeV.

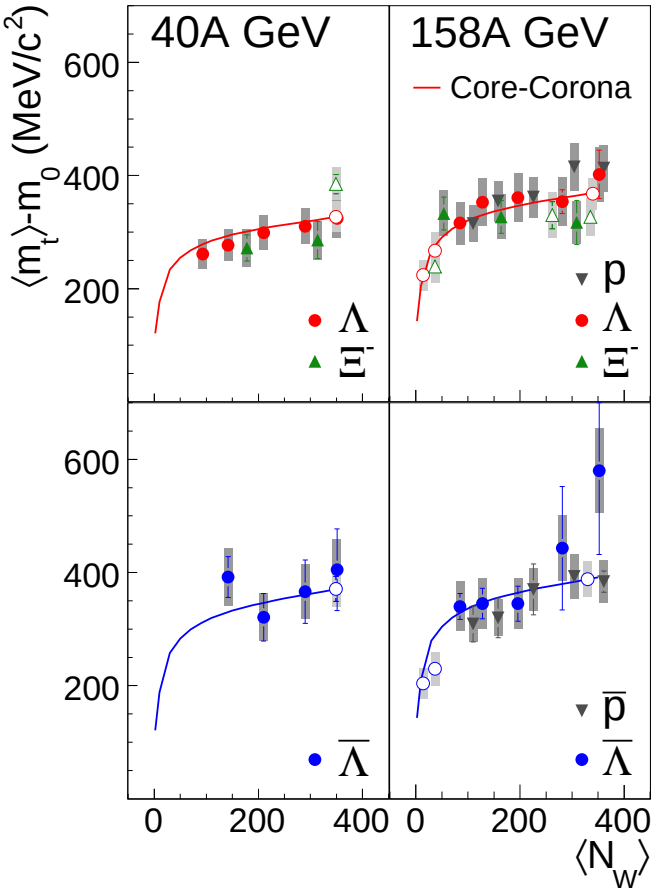

FIG. 6: (color online) The $\langle m_t \rangle - m_0$ values at mid-rapidity (p/$\bar{p}$: -0.5 < y < -0.1, $\Lambda/\bar{\Lambda}$: $|y| < 0.4$, Ξ^-: $|y| < 0.5$) for Pb+Pb collisions at 40A and 158A GeV, as well as for near-central C+C and Si+Si reactions at 158A GeV. The systematic errors are represented by the gray boxes. The filled symbols correspond to the results obtained from the minimum bias data sets, while the open ones represent the (near-)central reaction systems. The (anti-)proton data are taken from [27]. Also shown are the results from a fit for Λ and $\bar{\Lambda}$ with the core-corona approach (solid lines).

The m_t spectra were fitted by an exponential as defined in Eq. (1) in the transverse mass range $m_t - m_0 >$ 0.2 GeV/c^2 (Pb+Pb data) and $m_t - m_0 > 0.0$ GeV/c^2 (C+C and Si+Si data). The resulting inverse slope parameters T are listed in Tables IV, V, and VI.

For a model independent study of the energy dependence of m_t spectra, the average transverse mass $\langle m_t \rangle - m_0$ was calculated. To account for the unmeasured m_t range two different parametrizations were employed to extrapolate: an exponential function (shown in Figs. 4 and 5) and a blast-wave function [26] (not shown). Both provide a good description of the measured data. An estimate of the systematic error is derived from the differences between the two approaches. The resulting values for $\langle m_t \rangle - m_0$ are listed in Tables IV, V, and VI.

Figure 6 shows the dependence of $\langle m_t \rangle - m_0$ on $\langle N_w \rangle$ for the hyperon data compared to previously published proton and antiproton results [27]. The mass differences between the shown particle species are not very large and their $\langle m_t \rangle - m_0$ values agree within errors for each particular collision system. However, there is a significant system-size dependence. A strong increase is observed for $\langle N_w \rangle$ below 60, whereas above this region the values of $\langle m_t \rangle - m_0$ rise slowly with centrality in Pb+Pb collisions.

B. Rapidity spectra

The rapidity spectra of Λ and $\bar{\Lambda}$ for Pb+Pb collisions at 40A and 158A GeV are summarized in Figs. 7 and 8. For Ξ^- the statistics of the minimum bias datasets was not sufficient to extract rapidity spectra. While the Λ distributions at 40A GeV and the $\bar{\Lambda}$ distributions at 40A and 158A GeV have a Gaussian shape at all centralities, the Λ distributions at 158A GeV are rather flat over the measured rapidity range, similar to what has been observed for central Pb+Pb reactions [8]. The Λ and $\bar{\Lambda}$ spectra for the near-central C+C and Si+Si collisions are shown in Fig. 9. Also here the rapidity distributions for Λ are relatively flat with an indication for a minimum at mid-rapidity, which appears to be even more pronounced than in the case of the Pb+Pb data. The corresponding rapidity densities dN/dy around mid-rapidity for all data sets are listed in Tables IV, V, and VI.

The determination of total multiplicities requires an extrapolation into the unmeasured y regions. For this purpose the Λ distributions at 40A GeV were fitted with the sum of two Gauss functions of equal width σ which are displaced symmetrically by s with respect to mid-rapidity:

$$\frac{\mathrm{d}N}{\mathrm{d}y} \propto \exp\left\{-\frac{(y-s)^2}{2\sigma^2}\right\} + \exp\left\{-\frac{(y+s)^2}{2\sigma^2}\right\}. \qquad (2)$$

At 158A GeV, the data do not allow to determine the shape of the Λ rapidity spectra outside the plateau region around mid-rapidity. We therefore use the same assumptions on the spectral shape that have been applied to the central Pb+Pb data at 158A GeV [8] for all centrality bins in order to extract total multiplicities. This, of course, assumes that the widths of the rapidity distributions do not change substantially with centrality. For the $\bar{\Lambda}$ spectra a single Gaussian provides a reasonable fit at both beam energies.

The fitted RMS_y values are tabulated in Tables IV, V, and VI. Figure 10 displays the system-size dependence of RMS_y. While for Λ at 40A GeV an indication for a decrease of the widths with increasing centrality can be seen, no significant system-size dependence is observed for $\bar{\Lambda}$ at both beam energies.

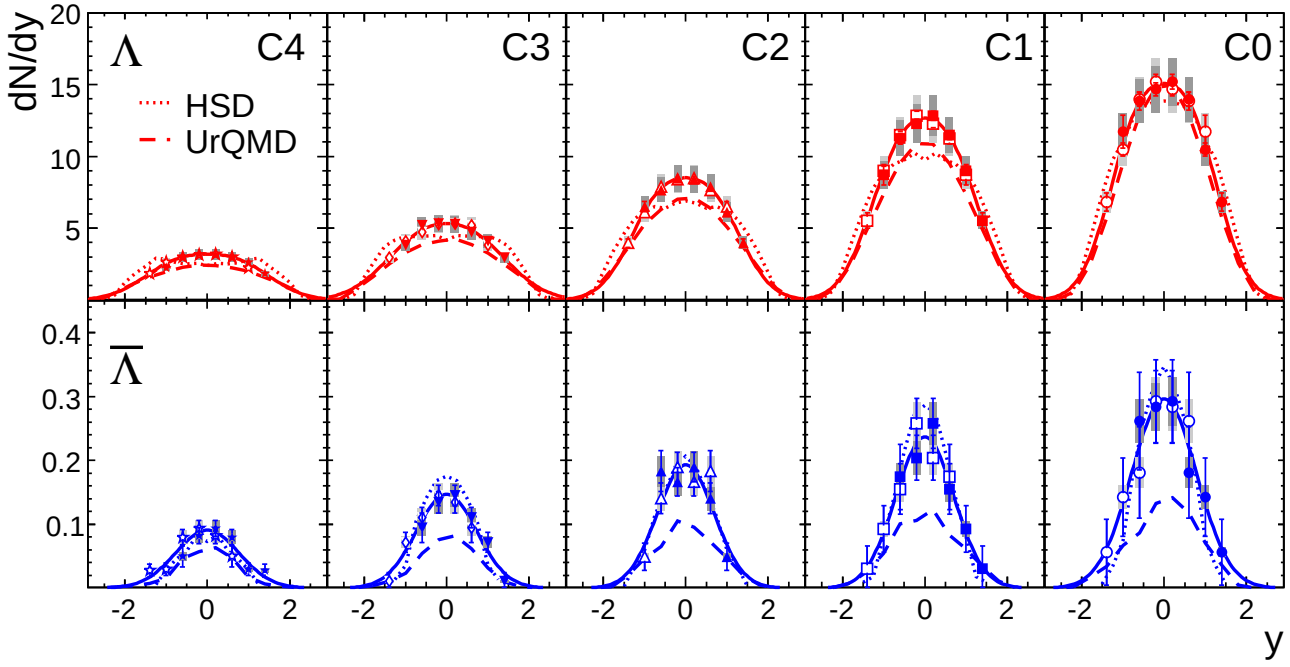

FIG. 7: (color online) The rapidity spectra of Λ and $\bar{\Lambda}$ for Pb+Pb collisions at 40A GeV for the 5 different centrality bins C0 – C4. The open symbols show data points reflected around mid-rapidity. The systematic errors are represented by the gray boxes. Solid lines are fits to the data points, used to extrapolate the measurements in order to extract total yields. Also included are calculations with the HSD model [30, 31, 32] (dotted lines) and the UrQMD2.3 model [33, 34, 35] (dashed lines).

C. Particle yields

Figure 11 shows the system-size dependences of the rapidity densities dN/dy at mid-rapidity for Λ, $\bar{\Lambda}$, and Ξ^-, divided by the average number of wounded nucleons $\langle N_w \rangle$. For $\langle N_w \rangle > 60$, dN/dy/$\langle N_w \rangle$ of Λ is almost independent of the system size, while for smaller systems at 158A GeV, corresponding to a $\langle N_w \rangle$ range not covered by Pb+Pb collisions, a significant rise with $\langle N_w \rangle$ is observed. However, one should keep in mind that a direct comparison of near-central C+C and Si+Si reactions to peripheral Pb+Pb collisions is complicated by the fact that the surface to volume ratio of these reaction systems is different. In the case of $\bar{\Lambda}$, this ratio seems to be independent from the system size even for very small systems. The Ξ^-, on the other hand, exhibits a weak $\langle N_w \rangle$ dependence. For comparison, data of the NA57 collaboration are also included in Fig. 11. Generally, the dN/dy values of NA57 are higher for non-central Pb+Pb collisions, similar to what has already been found for central Pb+Pb [8]. It appears, however, that the discrepancy becomes smaller for peripheral collisions.

The total multiplicities $\langle N \rangle$ of Λ and $\bar{\Lambda}$ at 40A and 158A GeV, as determined from extrapolations of the rapidity spectra shown in Figs. 7, 8, and 9 normalized by $\langle N_w \rangle$ are summarized in Fig. 12. A similar picture emerges as for the mid-rapidity dN/dy values. In the range $\langle N_w \rangle > 60$ the ratio $\langle N \rangle / \langle N_w \rangle$ is independent of the system size. Towards smaller system sizes, covered only by C+C and Si+Si collisions at 158A GeV, a significant decrease for Λ is observed, while in case of the $\bar{\Lambda}$ this ratio remains constant throughout.

IV. DISCUSSION

A. Comparison to transport models

Transport models allow to study several effects that may influence the system size dependence of strange particle production, e.g. multi-meson fusion processes, absorption of anti-baryons in the fireball, and the evolution of the longitudinal distribution of baryon number.

Multi-meson fusion processes are a possible mechanism to enhance the production of anti-baryons [28] and may therefore be important for reaching statistical equilibrium yields of multi-strange anti-baryons [29]. The HSD model [30, 31, 32] offers the possibility to include these fusion processes. The Figures 11 and 12 show comparisons of HSD and UrQMD2.3 [33, 34, 35] to the measured yields at mid-rapidity and to the total yields. For Λ the predictions of both models are close to the data. However, the system-size dependence, especially for the total yields, seems to be better described by HSD. The multi-meson fusion processes are naturally most important for $\bar{\Lambda}$. This explains why the spectra and yields for $\bar{\Lambda}$ in Pb+Pb predicted by HSD are higher than those from UrQMD2.3, which does not feature these processes. HSD

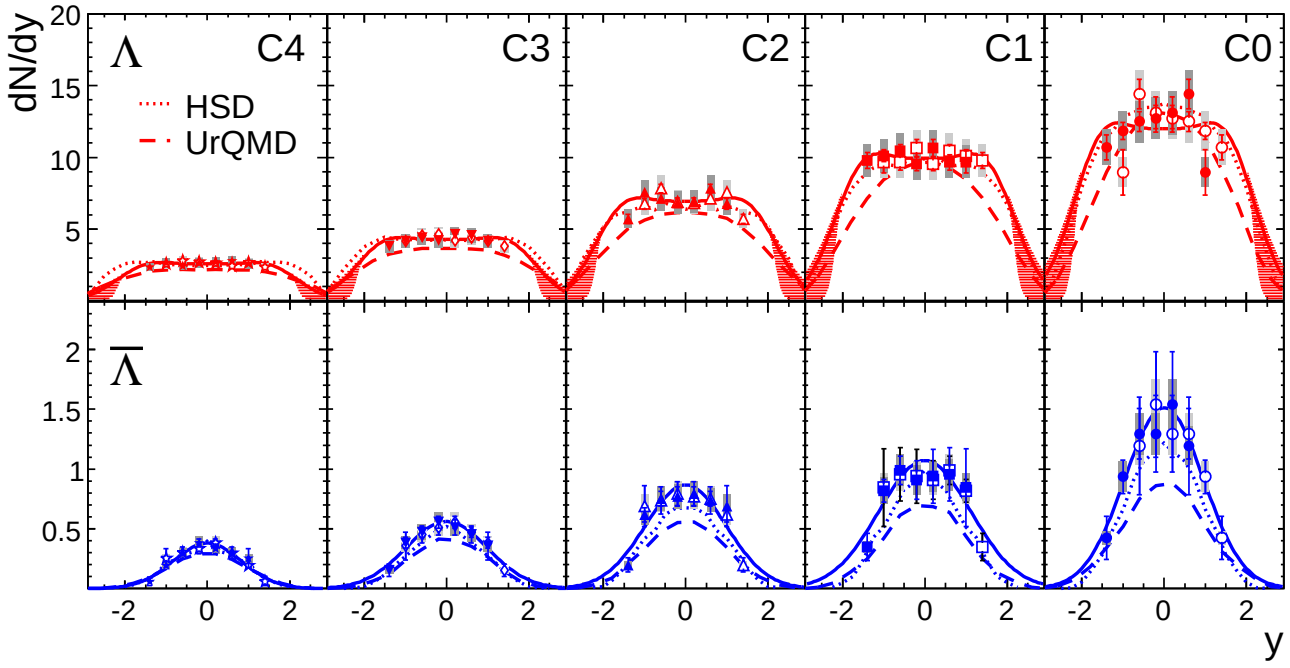

FIG. 8: (color online) The rapidity spectra of Λ and $\bar{\Lambda}$ for Pb+Pb collisions at 158A GeV in 5 different centrality bins C0 – C4. The open symbols show data points reflected around mid-rapidity. The systematic errors are represented by the gray boxes. Solid lines are fits to the data points, used to extrapolate the measurements in order to extract total yields. The shaded areas in the Λ spectra sketches the uncertainty due to the different extrapolations. Also included are calculations with the HSD model [30, 31, 32] (dotted lines) and the UrQMD2.3 model [33, 34, 35] (dashed lines).

gives thus a better description of the measurements. The yield of Ξ^- is underestimated by UrQMD2.3 by factors of 2 – 3 for all systems. No HSD calculations for the Ξ^- are available yet.

The system-size dependence of anti-baryon yields should also be affected by their possible absorption in the surrounding dense matter of the fireball. In this case one would expect the measured $\bar{\Lambda}$ yield per wounded nucleon to go down when comparing the small C+C and Si+Si systems with central Pb+Pb collisions. In fact, the data on $\langle N\rangle/\langle N_{\rm w}\rangle$ for $\bar{\Lambda}$ at 158A GeV seem to exhibit the expected tendency to decrease from C+C towards Pb+Pb collisions (see Fig. 12d), quite in contrast to the Λ, where $\langle N\rangle/\langle N_{\rm w}\rangle$ is rather increasing in the region $\langle N_{\rm w}\rangle < 60$ (see Fig. 12b). A similar behavior is predicted by UrQMD2.3, where it is, however, stronger at 40A GeV than at 158A GeV. But due to the size of the systematic error of the measurements, no final conclusion can be made whether $\bar{\Lambda}$ production is really affected by absorbtion.

Figures 7, 8, and 9 include a comparison of the transport model predictions to the measured rapidity distributions of Λ and $\bar{\Lambda}$. In the case of $\bar{\Lambda}$ the predicted widths of the rapidity distributions from both models, UrQMD2.3 and HSD, fit the data for all studied systems and energies reasonably well (see Fig. 10). Λ rapidity spectra, which are sensitive to the final distribution of baryon number, exhibit a significant dependence of their shape on system size. Also here the agreement to the models is fairly good at both energies, even though UrQMD2.3 predicts a Gaussian shaped distribution at 158A GeV, while the data would rather suggest a plateau inside the measured region. HSD, on the other hand, describes this flat shape relatively well. Similar observations have been made in the case of proton rapidity distributions in minimum bias Pb+Pb reactions at 158A GeV, where HSD also gives a better agreement with the observed flat proton spectra than UrQMD2.3 [36]. The reason for this difference lies in a different assumption on when a nucleon is allowed to interact again after its first collision. On top of a formation time of $\tau = 0.8$ fm/c, which is implemented in both models, HSD requires that the local energy density falls below 1 GeV/fm^3, which is considered as the critical energy density for a phase transition to a QGP. Thus, the data would suggest that this additional criterion is needed to properly describe the redistribution of baryon number in longitudinal phase space due to stopping.

B. Core-Corona approach

In order to compare the core-corona approach with the data presented here, we generalize the prescription given in [18] and parametrize the system-size dependence of any observable X by:

$$X(\langle N_{\rm w}\rangle) = \langle N_{\rm w}\rangle \left[f(\langle N_{\rm w}\rangle)\, X_{\rm core} + (1 - f(\langle N_{\rm w}\rangle))\, X_{\rm corona} \right] \quad (3)$$

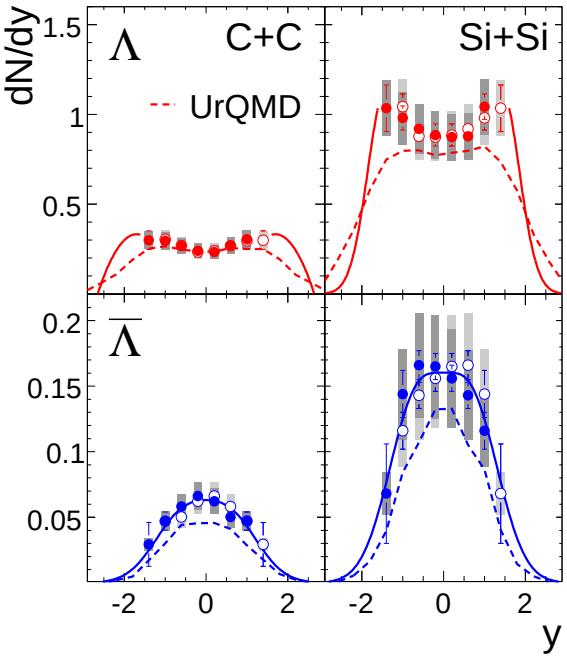

FIG. 9: (color online) The rapidity spectra of Λ and $\bar{\Lambda}$ for near-central C+C and Si+Si collisions at 158A GeV (the Λ spectra have already been published in [9]). Open symbols show data points reflected around mid-rapidity, while the systematic errors are represented by the gray boxes. Solid lines are fits to the data points, used to extrapolate the measurements in order to extract total yields. Also included are calculations with the UrQMD2.3 model [33, 34, 35] (dashed lines).

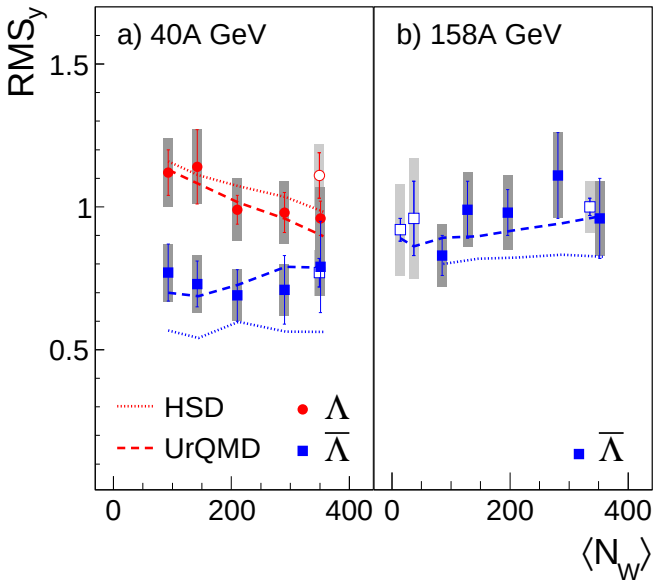

FIG. 10: (color online) The RMS widths of the rapidity distributions RMS_y of Λ and $\bar{\Lambda}$ at 40A and 158A GeV as a function of the number of wounded nucleons $\langle N_w \rangle$. The systematic errors are represented by the gray boxes. Filled symbols correspond to centrality selected data, obtained with a minimum bias trigger, while the open ones represent the reaction systems measured with a (near-)central trigger. Also included are calculations with the HSD model [30, 31, 32] (dotted lines) and the UrQMD2.3 model [33, 34, 35] (dashed lines).

The quantity X can either be the average transverse mass $\langle m_t \rangle - m_0$, the rapidity density dN/dy, or the total multiplicity $\langle N \rangle$. The function $f(\langle N_w \rangle)$ is here defined as the fraction of all participating nucleons, which interact more than once, and can therefore be attributed to the core region. Since the corona should behave like independent nucleon–nucleon collisions, the quantity X_{corona} corresponds to results of measurements in p+p collisions. Thus, the function $f(\langle N_w \rangle)$ provides a natural interpolation between p+p and Pb+Pb reactions. We use values for $f(\langle N_w \rangle)$ (see Table I), that have been calculated within a Glauber approach for Pb+Pb collisions at 158A GeV and have also been used in the toy model comparison discussed in [18]. Since the nucleon–nucleon cross section changes only slightly between 40 and 158 GeV beam energy, we use the same values of $f(\langle N_w \rangle)$ for the comparison to the 40A GeV data. It should be noted, though, that the direct comparison of the curves shown here to semi-central C+C and Si+Si collisions is not entirely correct, since their surface to volume ratio is different from that in Pb+Pb collisions. This, in principle, would require a calculation of $f(\langle N_w \rangle)$ specifically for these reaction systems. More insight could also be gained by studying the smaller systems in several centrality bins, similar to the study of Cu+Cu in [17]. However, our available statistics for C+C and Si+Si unfortunately does not allow this.

Based on the above recipe, the system-size dependence of $\langle m_t \rangle - m_0$ for Λ and $\bar{\Lambda}$ was constructed (solid lines in Fig. 6). The $\langle m_t \rangle - m_0$ values for Λ in p+p collisions are based on an interpolation of p+p data measured at various beam energies [38]. The p+p value for $\bar{\Lambda}$ was assumed to be the same as for Λ, since not enough data is available to do the extrapolation. The core contributions to $\langle m_t \rangle - m_0$ were adjusted to the measurements for central Pb+Pb collisions. In fact, the model provides a reasonable description of the measured system-size dependence in all cases.

Similarly, the system-size dependence of $dN/dy/\langle N_w \rangle$ and $\langle N \rangle / \langle N_w \rangle$ can be predicted using the core-corona approach as given by Eq. (3). The solid lines in Figs. 11 and 12 are based on the same function $f(\langle N_w \rangle)$ as has been used for $\langle m_t \rangle - m_0$. Here, X_{corona} is adjusted to the yields derived from an interpolation of Λ and $\bar{\Lambda}$ yields measured in p+p collisions at different beam energies [39]. For the Ξ^- at 158A GeV a preliminary p+p measurement by NA49 was used [40], while for 40A GeV no p+p input is available so that no comparison to Ξ^- is possible at this energy. X_{core} is defined in all cases by the measured dN/dy, resp. $\langle N \rangle$, for central Pb+Pb collisions. The agreement is good for the yields of Λ and

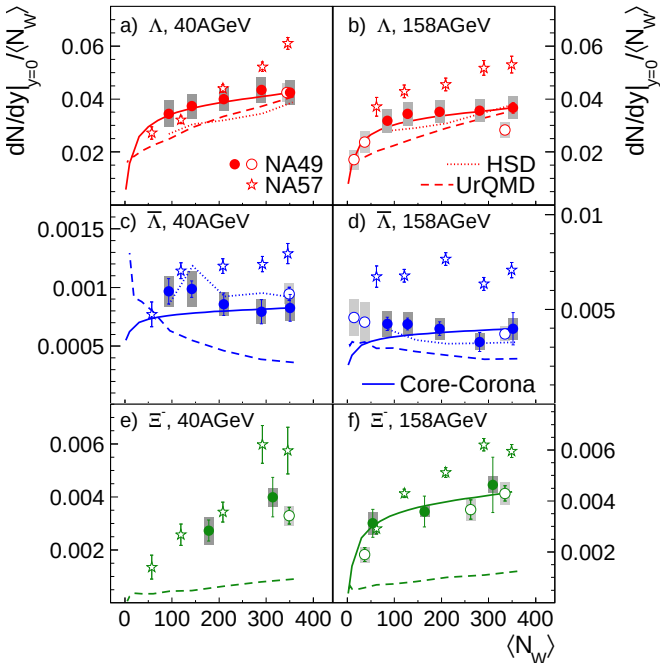

FIG. 11: (color online) The rapidity densities $\mathrm{d}N/\mathrm{d}y$ divided by the average number of wounded nucleons $\langle N_\mathrm{w}\rangle$ of Λ, $\bar{\Lambda}$, and Ξ^- at mid-rapidity ($\Lambda/\bar{\Lambda}$: $|y| < 0.4$, Ξ^-: $|y| < 0.5$) for Pb+Pb collisions at 40A and 158A GeV, as well as for near-central C+C and Si+Si reactions at 158A GeV, as a function of $\langle N_\mathrm{w}\rangle$. The systematic errors are represented by the gray boxes. Filled symbols correspond to the minimum bias trigger, while the open ones represent the online triggered (near-)central reaction systems. Also shown are data of the NA57 collaboration [5, 37] (open stars) and calculations with the HSD model [30, 31, 32] (dotted lines), the UrQMD2.3 model [33, 34, 35] (dashed lines), and the core-corona approach (solid lines).

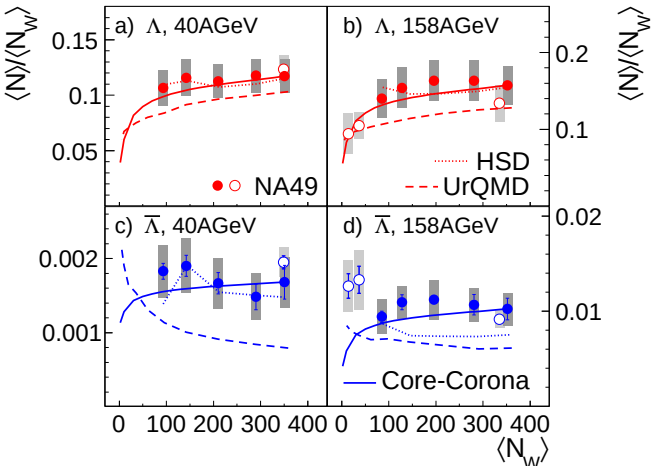

FIG. 12: (color online) The total multiplicities $\langle N\rangle$ divided by the average number of wounded nucleons $\langle N_\mathrm{w}\rangle$ of Λ and $\bar{\Lambda}$ for Pb+Pb collisions at 40A and 158A GeV, as well as for near-central C+C and Si+Si reactions at 158A GeV, as a function of $\langle N_\mathrm{w}\rangle$. The systematic errors are represented by the gray boxes. Filled symbols correspond to the minimum bias trigger, while the open ones represent online triggered (near-)central reaction systems. Also shown are calculations with the HSD model [30, 31, 32] (dotted lines), the UrQMD2.3 model [33, 34, 35] (dashed lines), and the core-corona approach (solid lines).

Ξ^- (see: Figs. 11 and 12). However, for $\bar{\Lambda}$ at 158A GeV the yields measured in C+C and Si+Si collisions are at the same level as for Pb+Pb reactions. This behaviour cannot be fitted by the core-corona approach and would therefore indicate that also other mechanisms, such as $\bar{\Lambda}$-absorption, need to be taken into account to arrive at a proper description of the system-size dependence.

V. SUMMARY

A measurement of Λ, $\bar{\Lambda}$, and Ξ^- production in centrality selected Pb+Pb collisions at 40A and 158A GeV and in near-central C+C and Si+Si collisions at 158A GeV is presented. The first moments of the transverse mass spectra ($\langle m_\mathrm{t}\rangle - m_0$) exhibit only a weak system-size dependence for $\langle N_\mathrm{w}\rangle > 60$, while for the small systems a rapid rise of $\langle m_\mathrm{t}\rangle - m_0$ with increasing system size is observed. The rapidity distributions of Λ at 40A GeV and of $\bar{\Lambda}$ at 40A and 158A GeV have a Gaussian shape. For Λ at 158A GeV the rapidity spectra are rather flat in the measured region $-1.6 < y < 1.2$. Generally, no pronounced system-size dependence of the widths of the rapidity distributions is observed. Only the Λ spectra at 40A GeV might show some indication for a slight narrowing with increasing centrality. The measured $\mathrm{d}N/\mathrm{d}y/\langle N_\mathrm{w}\rangle$ and $\langle N\rangle/\langle N_\mathrm{w}\rangle$ values rise rapidly with system size for small systems ($\langle N_\mathrm{w}\rangle < 60$) and do not change very much any more from then on. The core-corona approach describes the system-size dependence of $\langle m_\mathrm{t}\rangle - m_0$ for all particle species discussed here. It also reproduces the system-size dependence of the mid-rapidity $\mathrm{d}N/\mathrm{d}y$ values and of the total multiplicities of Λ and Ξ^-. However, the $\bar{\Lambda}$ spectra measured for C+C and Si+Si collisions at 158A GeV suggest a flatter system-size dependence than expected in the core-corona picture. Generally, the results of the hadronic transport models UrQMD2.3 and HSD for Λ and $\bar{\Lambda}$ are close to the data, with the exception of the underprediction of the absolute $\bar{\Lambda}$ yields at both energies by UrQMD2.3. But both models predict a system-size dependence of the $\bar{\Lambda}$ total multiplicity similar to the measurement. This might indicate that absorption of $\bar{\Lambda}$ in the dense hadronic medium, which is taken into account in the hadronic transport models, has a visible effect. However, these models are not able to describe the production of baryons with multiple strangeness. UrQMD2.3, for example, underestimates the yields of Ξ^- to a large extent (factor 2 – 3). The HSD model seems to provide a better description of the Λ rapidity spectra than UrQMD2.3 due to an im-

proved implementation of the stopping mechanism.

Acknowledgments

This work was supported by the US Department of Energy Grant DE-FG03-97ER41020/A000, the Bundesministerium für Bildung und Forschung, Germany (06F137), the Virtual Institute VI-146 of Helmholtz Gemeinschaft, Germany, the Hungarian Scientific Research Foundation (T032648, T032293, T043514), the Hungarian National Science Foundation, OTKA, (F034707), the Polish-German Foundation, the Polish Ministry of Science and Higher Education (1 P03B 006 30, 1 P03B 127 30, 0297/B/H03/2007/33, N N202 078735), the Korea Research Foundation (KRF-2007-313-C00175) and the Bulgarian National Science Fund (Ph-09/05).

[1] J. Rafelski and B. Müller, Phys. Rev. Lett. **48**, 1066 (1982).
[2] J. Bartke et al. (NA35 Collaboration), Z. Phys. C **48**, 191 (1990).
[3] T. Alber et al. (NA35 Collaboration), Z. Phys. C **64**, 195 (1994).
[4] F. Antinori et al. (WA97 Collaboration), Eur. Phys. J. C **11**, 79 (1999).
[5] F. Antinori et al. (NA57 Collaboration), J. Phys. G **32**, 427 (2006).
[6] L. Ahle et al. (E802 Collaboration), Phys. Rev. C **60**, 044904 (1999).
[7] P. Chung et al. (E895 Collaboration), Phys. Rev. Lett. **91**, 202301 (2003).
[8] C. Alt et al. (NA49 Collaboration), Phys. Rev. C **78**, 034918 (2008).
[9] C. Alt et al. (NA49 Collaboration), Phys. Rev. Lett. **94**, 052301 (2005).
[10] J. Rafelski and M. Danos, Phys. Lett. B **97**, 279 (1980).
[11] S. Hamieh, K. Redlich, and A. Tounsi, Phys. Lett. B **486**, 61 (2000).
[12] C. Höhne, F. Pühlhofer, and R. Stock, Phys. Lett. B **640**, 96 (2006).
[13] K. Werner, Phys. Rev. Lett. **98**, 152301 (2007).
[14] R.J. Glauber, Phys. Rev. **100**, 242 (1955).
[15] F. Becattini and J. Manninen, J. Phys. G **35**, 104013 (2008).
[16] F. Becattini and J. Manninen, Phys. Lett. B **673**, 19 (2009).
[17] A.R. Timmins (for the STAR Collaboration), arXiv:0810.0017.
[18] J. Aichelin and K. Werner, arXiv:0810.4465.
[19] S. V. Afanasiev et al. (NA49 Collaboration), Nucl. Instrum. Meth. A **430**, 210 (1999).
[20] W.-M. Yao et al. (Particle Data Group), J. Phys. G **33**, 1 (2006).
[21] K. Werner, Phys. Rept. **232**, 87 (1993).
[22] Geant—Detector Description and Simulation Tool, CERN Program Library Long Writeup W5013.
[23] I. Kraus, PhD thesis, University of Frankfurt (2004).
[24] M. K. Mitrovski, PhD thesis, University of Frankfurt (2007).
[25] F. Becattini, J. Manninen, and M. Gaździcki, Phys. Rev. C **73**, 044905 (2006).
[26] E. Schnedermann and U. Heinz, Phys. Rev. C **50**, 1675 (1994).
[27] T. Anticic et al. (NA49 Collaboration), Phys. Rev. C **69**, 024902 (2004).
[28] W. Cassing, Nucl. Phys. A **700**, 618 (2002).
[29] C. Greiner and S. Leupold, J. Phys. G **27**, L95 (2001).
[30] W. Ehehalt and W. Cassing, Nucl. Phys. A **602**, 449 (1996).
[31] W. Cassing and E.L. Bratkovskaya, Phys. Rep. **308**, 65 (1999).
[32] H. Weber, E.L. Bratkovskaya, W. Cassing, and H. Stöcker, Phys. Rev. C **67**, 014904 (2003), and private communication.
[33] M. Bleicher et al, J. Phys. G **25**, 1859 (1999).
[34] H. Petersen, M. Bleicher, S. A. Bass, and H. Stöcker, arXiv:0805.0567.
[35] H. Petersen, M. Mitrovski, T. Schuster, and M. Bleicher, arXiv:0903.0396.
[36] C. Blume et al. (for the NA49 Collaboration), PoS(Confinement08), **110** (2008), and NA49 publication in preparation.
[37] F. Antinori et al. (NA57 Collaboration), Phys. Lett. B **595**, 68 (2004).
[38] F. Kramer, C. Strabel, and M. Gaździcki, arXiv:nucl-ex/0509035.
[39] M. Gaździcki and D. Röhrich, Z. Phys. C **71**, 55 (1996).
[40] T. Šuša (for the NA49 Collaboration), Nucl. Phys. A **698**, 491c (2002).

APPENDIX A: TABLES

TABLE IV: The rapidity densities at mid-rapidity ($\Lambda/\bar{\Lambda}$: $|y| < 0.4$, Ξ^-: $|y| < 0.5$), the total multiplicities $\langle N \rangle$, the RMS widths of the rapidity distributions $RMS_{\rm y}$ calculated from the fits shown in Fig. 7, the average transverse masses $\langle m_{\rm t} \rangle - m_0$, and the inverse slope parameters T for Pb+Pb collisions at 40A GeV. The first error is statistical, the second systematic.

	Centrality class	$\langle N_{\rm w} \rangle$	dN/dy	$\langle N \rangle$	$RMS_{\rm y}$	$\langle m_{\rm t} \rangle - m_0$ (MeV/c^2)	T (MeV)
Λ	0	351±3	14.9±0.3±1.6	41.1±0.8±5.3	0.96±0.06±0.11	324±10±33	268± 7±16
	1	290±4	12.6±0.2±1.4	34.1±0.6±4.4	0.98±0.07±0.11	310± 8±31	256± 4±15
	2	210±6	8.4±0.1±0.9	23.6±0.3±3.1	0.99±0.05±0.11	299± 6±30	247± 3±15
	3	142±8	5.3±0.1±0.6	16.4±0.2±2.1	1.14±0.13±0.13	277± 6±28	230± 4±14
	4	93±7	3.2±0.05±0.4	9.9±0.1±1.3	1.12±0.08±0.12	261± 6±26	220± 5±13
$\bar{\Lambda}$	0	351±3	0.29±0.04±0.04	0.59±0.08±0.12	0.79±0.16±0.10	405±72±53	325±81±32
	1	290±4	0.23±0.03±0.03	0.43±0.05±0.09	0.71±0.12±0.09	366±56±48	299±40±30
	2	210±6	0.18±0.02±0.02	0.35±0.03±0.07	0.69±0.09±0.09	321±42±42	276±38±28
	3	142±8	0.14±0.01±0.02	0.27±0.02±0.05	0.73±0.08±0.10	392±36±51	346±69±35
	4	93±7	0.09±0.01±0.01	0.17±0.01±0.03	0.77±0.10±0.10	—	—
Ξ^-	0–1	314±4	1.25±0.23±0.14	—	—	286±33±34	232±19±14
	2–3	178±8	0.49±0.07±0.05	—	—	272±23±33	233±18±14

TABLE V: The rapidity densities at mid-rapidity ($\Lambda/\bar{\Lambda}$: $|y| < 0.4$, Ξ^-: $|y| < 0.5$), the total multiplicities $\langle N \rangle$, the RMS widths of the rapidity distributions $RMS_{\rm y}$ calculated from the fits shown in Fig. 8, the average transverse masses $\langle m_{\rm t} \rangle - m_0$, and the inverse slope parameters T for Pb+Pb collisions at 158A GeV. The first error is statistical, the second systematic.

	Centrality class	$\langle N_{\rm w} \rangle$	dN/dy	$\langle N \rangle$	$RMS_{\rm y}$	$\langle m_{\rm t} \rangle - m_0$ (MeV/c^2)	T (MeV)
Λ	0	352±3	12.9±0.7±1.5	55.3±1.8±8.8	—	402±43±48	346±34±21
	1	281±4	10.0±0.4±1.2	45.9±1.0±7.3	—	354±21±43	296±14±18
	2	196±6	6.9±0.2±0.8	32.0±0.5±5.1	—	361±16±43	307±11±18
	3	128±8	4.4±0.1±0.5	19.7±0.3±3.2	—	353±15±42	303±12±18
	4	85±7	2.7±0.1±0.3	11.9±0.2±1.9	—	316±14±38	274±15±16
$\bar{\Lambda}$	0	352±3	1.4±0.3±0.2	3.6±0.4±0.6	0.96±0.14±0.13	580±148±75	507±211±51
	1	281±4	0.92±0.14±0.12	3.0±0.3±0.5	1.11±0.15±0.15	443±109±58	372±62±37
	2	196±6	0.78±0.07±0.11	2.2±0.1±0.4	0.98±0.08±0.13	345±31±45	296±27±30
	3	128±8	0.54±0.04±0.07	1.4±0.1±0.2	0.99±0.10±0.13	345±27±45	302±34±30
	4	85±7	0.36±0.03±0.05	0.8±0.05±0.14	0.83±0.07±0.11	340±23±44	309±50±31
Ξ^-	0–1	309±4	1.43±0.33±0.16	—	—	317±39±38	244±41±15
	2–3	164±8	0.59±0.10±0.06	—	—	327±29±39	264±39±16
	4–5	54±7	0.17±0.03±0.02	—	—	333±29±40	261±37±16
	0–2	262±4	0.96±0.10±0.11	—	—	330±24±40	263±14±16

TABLE VI: The rapidity densities at mid-rapidity ($\Lambda/\bar{\Lambda}$: $|y| < 0.4$, Ξ^-: $|y| < 0.5$), the total multiplicities $\langle N \rangle$, the RMS widths of the rapidity distributions $RMS_{\rm y}$ calculated from the fits shown in Fig. 9, the average transverse masses $\langle m_{\rm t} \rangle - m_0$, and the inverse slope parameters T for near-central C+C and Si+Si collisions at 158A GeV. The first error is statistical, the second systematic.

	Reaction system	$\langle N_{\rm w} \rangle$	dN/dy	$\langle N \rangle$	$RMS_{\rm y}$	$\langle m_{\rm t} \rangle - m_0$ (MeV/c^2)	T (MeV)
Λ	C+C	14±2	0.24 ±0.01±0.04	1.32±0.05±0.32	—	224± 6±27	199± 8±15
	Si+Si	37±3	0.88 ±0.04±0.13	3.88±0.16±0.56	—	267±16±32	235± 9±16
$\bar{\Lambda}$	C+C	14±2	0.064±0.003±0.010	0.18±0.02±0.03	0.92±0.04±0.16	204± 9±27	184±11±17
	Si+Si	37±3	0.16 ±0.007±0.038	0.49±0.05±0.11	0.96±0.13±0.21	230±10±30	205± 9±17
Ξ^-	Si+Si	37±3	0.07 ±0.01 ±0.01	—	—	239±16±29	210±13±13